

Bodur, Ö., Göğüş, O. H., Brune, S., Şengül
Uluocak, E., Glerum, A., Fichtner, A., Sözbilir, H.
(2023): Crustal flow driving twin domes
exhumation and low-angle normal faulting in the
Menderes Massif of western Anatolia. - Earth and
Planetary Science Letters, 619, 118309.

<https://doi.org/10.1016/j.epsl.2023.118309>

Crustal flow driving twin domes exhumation and low angle normal faulting in the Menderes Massif of western Anatolia

Ömer Bodur^{1,2}, Oğuz Hakan Göğüş¹, Sascha Brune³, Ebru Şengül Uluocak⁴, Anne Glerum³, Andreas Fichtner⁵, Hasan Sözbilir⁶

¹ *Eurasia Institute of Earth Sciences, Istanbul Technical University, Istanbul, Turkey*

² *Department of Geosciences, The University of Texas at Dallas, Richardson, Dallas, 75080-3021, TX*

³ *Helmholtz-Centre Potsdam, GFZ German Research Centre for Geosciences, Telegrafenberg, D-14473, Potsdam, Germany*

⁴ *Department of Geophysical Engineering, Çanakkale Onsekiz Mart University, Çanakkale, Turkey*

⁵ *Department of Earth Sciences, ETH Zurich, Zurich, Switzerland*

⁶ *Department of Geology, Engineering Faculty, Dokuz Eylül University, Bornova-Izmir, Turkey*

1 **Abstract**

2 Lower crustal flow in regions of post-orogenic extension has been inferred to explain
3 the exhumation of metamorphic core complexes and associated low-angle normal
4 (detachment) fault systems. However, the origin of detachment faults, whether
5 initially formed as high-angle or low-angle shear zones, and the extension is
6 symmetric or asymmetric remains enigmatic. Here, we use numerical modeling
7 constrained by geophysical and geological data to show that symmetric extension in
8 the central Menderes Massif of western Anatolia is accommodated by the crustal
9 flow. Our geodynamic model explains how opposite dipping Gediz and Büyük
10 Menderes detachment faults are formed by $\sim 40^\circ$ footwall rotation. Model predictions
11 agree with seismic tomography data that suggests updoming of lower crust beneath
12 the exhumed massifs, represented as “twin domes” and a flat Moho. Our work helps
13 to account for the genetic relation between the exhumation of metamorphic core
14 complexes and low-angle normal faulting in both Cordillera and Aegean orogenic
15 regions and has important implications on crustal dynamics in extensional provinces.

16 *Keywords:* Geodynamic Modeling, Lower Crustal Flow, Western Anatolia

17 **1. Introduction**

18 Extensional tectonics following mountain building- orogenic- processes lead
19 to special geological characteristics of the crust, such as rapid pulses of magmatism,
20 exhumation of metamorphic core complexes, and associated low-angle normal
21 (detachment) faults with tens of kilometers of displacements (Lister et al., 1984;
22 Dewey, 1988; Malavieille, 1993; Jolivet, 2001; Rey et al., 2001). However, the extent
23 and magnitude to which post-orogenic extension is involved in strain localization in
24 the brittle upper crust and in ductile flow in the lower crust are not well understood. In
25 this work, we test the hypothesis that the origin of central Menderes metamorphic
26 core complex and symmetric detachment faulting in western Anatolia, a post-Alpine
27 extended region, are formed by ductile flow of lower crust and footwall rotation of
28 high-angle normal faults.

29 The exhumation of metamorphic rocks in the central Menderes Massif has
30 been accommodated by two symmetrically developed, outward-facing ductile-brittle
31 high strain (low-angle) detachment faults ($<20^\circ$). The northern detachment fault, the
32 Gediz/Alaşehir detachment, is associated with the top-to-the N-NNE shear sense,
33 whereas the southern one is associated with the top-to-the S shear sense (Hetzel et al.,
34 1995; Emre and Sözbilir, 1997; Gessner et al., 2001; Bozkurt, 2001; Lips et al., 2001;
35 Işık et al., 2003; Göğüş, 2004; Çemen et al., 2006; Nilius et al., 2019; Heineke et al.,
36 2019b) (Fig. 1a, b). Proposed ages for the initiation of normal faulting for each
37 detachment system vary spatially and temporally. For instance, based on isotopic
38 dating along fault rocks cataclasites, Hetzel et al. (2013), suggest that the onset of
39 Büyük Menderes detachment faulting is $\sim 22\text{-}20$ Ma, whereas the shearing across the
40 Gediz detachment began at ~ 16 Ma inferred from dating of syn-extensional intrusions
41 (Catlos and Çemen, 2005; Glodny and Hetzel, 2007; Rossetti et al 2017). Further,

42 magnetostratigraphic analysis and isotopic ages over the supra-detachment basins
43 suggest that these two detachments have operated simultaneously since 16 Ma (Şen
44 and Seyitoğlu, 2009). A detachment-controlled symmetric cooling pattern related to
45 unroofing of central Menderes has also been suggested through thermochronological
46 studies (Gessner et al 2001; Ring et al., 2003). Such symmetric configuration of core
47 complex exhumation has been interpreted with respect to the Küçük Menderes graben
48 (rift), located above a central axis of a large-scale syncline where both detachments
49 and the folding evolved contemporaneously (Gessner et al., 2001; Seyitoğlu et al.,
50 2004).

51 While strain localization across exhumed ranges in the central Menderes
52 Massif region is characterized by detachment faults, high-angle normal faults are well
53 documented along the graben boundaries - akin to rifted margins (Fig. 1a,b). Based on
54 field observations and seismic reflection data, a number of studies interpret that
55 detachment faults in central Menderes were initially formed at higher dip angles ($>$
56 30°) and rotated to shallower orientations (Cohen et al., 1995; Bozkurt, 2000; Gessner et
57 al., 2001; Seyitoğlu et al., 2002; Bozkurt and Sözbilir, 2004, Çiftci and Bozkurt, 2010;
58 Demircioğlu et al., 2010). Gessner et al (2001) propose a rolling-hinge model to address
59 the synchronous evolution of bivergent detachment fault systems. Namely, flexural
60 isostatic footwall uplift is associated with fault rotation as well as the formation of
61 younger high-angle normal faults on the hanging-wall of the main breakaway which
62 successively rotates to low-angle shear zones (Buck, 1988, Wernicke and Axen, 1988).
63 Accordingly, a rolling hinge type tectonic evolution for discrete shear zones in the
64 footwall of the Gediz (Alaşehir) detachment (Seyitoğlu et al., 2002) and the Büyük
65 Menderes detachment (Sümer et al 2020; Türesin and Seyitoğlu, 2021) has been invoked
66 through geologic mapping, stratigraphic analyses, and data from seismic reflection

67 studies. On the other hand, Öner and Dilek (2011) suggests that the detachment fault
68 was initially formed as a low angle shear zone (without rotation) in which the early
69 Miocene-late Pleistocene sediments of Alaşehir (Gediz) graben were deposited in a
70 supradetachment basin. While the studies above provide a conceptual geological
71 framework, however, the origin of core complex exhumation and evolution of ductile-
72 to-brittle localized strain have not been addressed in the context of whole-crust
73 extensional dynamics.

74 A multi-scale full seismic waveform inversion for crustal and upper-mantle
75 structures by Fichtner et al. (2013) demonstrates that the upper crust of the Menderes
76 Massif is associated with anomalously high velocities with respect to neighboring
77 regions. This has led to the interpretation of upward displacement of the lower crust
78 typically associated with higher velocities than the upper crust (Figure 1c). Seismic
79 analyses of Karabulut et al. (2013) also imply a flow of lower crust beneath the
80 central Menderes Massif, inferred from the locally flat Moho at ~25 km depth to
81 accommodate isostatic compensation through lower crustal dynamics (Block and
82 Royden, 1990). Further, a lower velocity upper crustal anomaly has been imaged
83 beneath the Küçük Menderes graben (Figure 1c) in addition to the updoming lower
84 crustal material shown in the relatively long-wavelength (> 150 km) variations of the
85 isotropic S velocities (Fichtner et al., 2013).

86 In this work, by using thermo-mechanical models we investigate the dynamics
87 of the post-orogenic extension where lower crustal flow plays a key role in strain
88 distribution. Specifically, the evolution of an array of high and low-angle normal
89 faults is explored and a genetic relationship between these faults and the exhumation
90 of lower crustal rocks is demonstrated. Further modeling is used to test the role of
91 varying extension rates and reduced upper crustal strength. Results are reconciled

92 with the last ~ 15 Ma evolution of the central Menderes Massif of western Anatolia,
93 where symmetrically arranged detachment systems are prominent and seismological
94 data suggests lower crustal flow. Overall, our work will provide new insight into how
95 crustal dynamics control the tectonics of rifted margins and the evolution
96 metamorphic core complexes around the globe.

97 **2. Data and Methods**

98 *2.1. Numerical technique, rheological characteristics, and model setup*

99 To reach the objectives of this work, we use the finite element code ASPECT
100 (Heister et al., 2017; Kronbichler et al., 2012), which has been extensively used for
101 conducting geodynamical experiments ranging in scale from the crust to the deeper
102 mantle. ASPECT is employed to solve the extended Boussinesq equations of
103 momentum, mass, and energy as well as advection equations for each compositional
104 field. We compute the 2-D visco-plastic deformation within the lithosphere and sub-
105 lithospheric mantle of a model domain that is 500 km wide and 165 km deep (Figure
106 2). Adaptive mesh refinement is used to adapt the precision and optimization of the
107 computational calculations. We employ coarse, intermediate, and maximum
108 resolutions beneath 50 km depth, between 50 and 20 km depth, and above 20 km
109 depth, each represented by a resolution of 2500, 1250, and 625 m respectively.

110 In terms of rheological setup, the visco-plastic effective viscosity η_{eff} is
111 computed from either a composite of dislocation and diffusion creep $\eta_{eff}^{diff|disl} =$
112 $\frac{1}{2} \left(\frac{1}{A}\right)^{1/n} \dot{\epsilon}_e^{(1-n)/n} \exp\left(\frac{Q+PV}{nRT}\right)$, or Drucker-Prager plasticity $\eta_{eff}^{pl} = \frac{C \cos(\phi) + P \sin(\phi)}{2 \dot{\epsilon}_e}$,
113 depending on whether viscous stresses remain smaller than the yield stress or not
114 (Glerum et al., 2018); with pressure P , temperature T , stress exponent $n = 1$ for

115 diffusion creep and $n > 1$ for dislocation creep, pre-exponential factor A , the effective
116 deviatoric strain rate $\dot{\epsilon}_e = \sqrt{\frac{1}{2} \dot{\epsilon}'_{ij} \dot{\epsilon}'_{ij}}$, activation energy Q , activation volume V , gas-
117 constant R , cohesion C , and friction angle ϕ (see Glerum et al., 2018 for numerical
118 implementation and our supplement for employed parameter values).

119 The initial conditions of our model design aim to approximate the first-order
120 lithospheric structure at the onset of extension in the central Menderes Massif region
121 of western Anatolia, approximately 15 million years ago. The model accounts for four
122 layers of materials: upper crust, lower crust, mantle lithosphere, and sub-lithospheric
123 mantle (Table 1 and Fig. 2). The crustal domain consists of an upper crust (25 km
124 thick) with wet quartzite rheology (Gleason & Tullis, 1995), and a lower crust (25 km
125 thick) with wet anorthite rheology (Figure 2) (Rybacki & Dresen, 2000). Our
126 assumption of an initial 50 km thick crust is based on geological inferences (e.g.,
127 paleoelevation and metamorphic grades of exhumed rocks) (Şengör et al., 1985) in
128 which extension in this region started after plate shortening by the Alpine orogeny. A
129 relatively thin (30 km thick) mantle lithosphere is included in the model setup with
130 dry olivine rheology (Hirth & Kohlstedt, 2003), since a number of geological studies
131 suggest that portions of mantle lithosphere have been removed from beneath the
132 region through lithospheric delamination or convective removal (Aldanmaz et al.,
133 2000; Ersoy et al., 2010; Van Hinsbergen et al., 2010; Gessner et al., 2013; Göğüş,
134 2015). The overall initial thickness of the lithosphere is 80 km.

135 ***2.2. Mechanical boundary conditions, thermal field and weakening effects***

136 Kinematic boundary conditions are implemented by prescribing half of the
137 extension velocity at each lateral model boundary. The top boundary is a free surface,

138 while the bottom boundary features a free tangential motion in conjunction with a
139 constant vertical inflow of material that balances the outflow through the lateral
140 model sides. A constant temperature is prescribed at the top (0°C) and bottom of the
141 model domain (1300°C), as well as isolating boundaries at the sides. The initial
142 temperature follows a steady-state geotherm in the lithosphere and an adiabat below.
143 Radiogenic, shear heating, and adiabatic heating are included in the energy equation.

144 We include strain weakening/softening, where a strain-dependent friction
145 angle and cohesion decrease linearly over a given strain interval (Huismans &
146 Beaumont, 2003; Le Pourhiet et al., 2017), which is also predicted in progressive
147 microscale numerical simulations (Dinç Gögüş et al., 2023). Here, the frictional
148 weakening factor for the upper crust is set to 0.1 (for EXP-1, 2, 3) or 0.05 (EXP-4)
149 over the accumulated plastic strain interval of 0 to 1. If strain exceeds 1, the friction
150 angle and cohesion remain constant at their most weakened value.

151 We show two model suites where we investigate the impact of key parameters
152 within a plausible range: (1) we vary the extension velocity between $V_{ext} = 1-4$
153 cm/year full rate and (2) we vary the friction angle strain weakening factor of the
154 upper crust (0.1 - 0.05).

155 **3. Results**

156 We show predictions of four experiments selected from a series of numerical
157 experiments (>100) in which the role of major controlling parameters on continental
158 extension is examined. Details on the model design, including the initial temperature
159 field and boundary conditions applied, are given in the methods section. Figure 2 and
160 Table 1 include further information on various parameters of the numerical
161 experiments. The description of the section below begins with an explanation of the

162 reference experiment (EXP-1) that best approximates the late Cenozoic geological
163 evolution of the central Menderes Massif and follows with presentations of EXP-2, 3,
164 and 4. Extension in the brittle crust begins through a random initial strain as a
165 representation of deformation distribution which further evolves into strain
166 localization. Results are only shown for the central part of the model domain, where
167 the respective approximate distances of the central Menderes to the plate boundaries
168 in the north and south are nearly close.

169 *3.1. Evolution of core complex and the low-angle (detachment) faults*

170 Figure 3 shows the evolution of our reference experiment EXP-1, where $V_{ext} =$
171 2 cm/yr extension rate has been applied, which approximates present-day GPS-
172 derived N-S extension in western Anatolia (Aktuğ et al., 2009). By 6 Myr (Fig. 3a),
173 strain is localized along opposing conjugate shear bands/fault systems, dipping 50°-
174 55° in the center of the model domain. Later by 12 Myr with more stretching (Fig.
175 3b), flow of the lower crust occurs where there is a higher magnitude of extension of
176 the upper crust, beneath two major faults, owing to the lateral lithostatic pressure
177 gradients. The net crustal thickness is now 30 km beneath the central region,
178 expressed as approximately flat Moho, while there is lower crustal thickening and
179 convergence beneath the zone of maximum upper crustal extension. The influx of
180 crustal material accommodates differential isostatic compensation, and upper portions
181 of the shear zone rotate to shallower dips around two domal/antiformal cores. By 15
182 Myr (Fig. 3c), more rocks from the deeper crust are dragged upward near the surface
183 along two major symmetrically (bivergent) arranged detachment systems, for
184 instance, lower crustal rocks are exhumed as shallow as <10 km depth below the
185 surface. The lowest dip angle of these faults near the surface is now ~11°-14° and
186 new high-angle normal faults develop on the hanging-wall of these main breakaway

187 fault systems. Note that the Moho variation is uniformly sub-horizontal (25 km)
188 beneath the central domain although thinning of the upper crust is heterogeneous. For
189 instance, there is a higher magnitude of stretching along upper (brittle) crustal
190 extension above detachment faults, and below that there is a culmination of a twin-
191 domes type core complex.

192 We test how variable rates of lithospheric extension can modify model
193 predictions on the timescale of 15 Myr. These results may provide insight into the
194 evolution of extensional tectonics both on the eastern and the western margin of the
195 central Menderes, where the former margin accounts for lower and the latter for
196 higher rates of extension due to its proximity to the central Aegean basin since
197 subduction retreat has caused back-arc spreading (Jolivet and Brun, 2010; Van
198 Hinsbergen et al., 2010a).

199 EXP-2 shows the model development in which the extension rate is halved
200 with respect to EXP-1 (so $V_{ext} = 1$ cm/yr) (Figure 4a). The vertical flow and
201 thickening of the lower crust and thinning of the upper crust are less pronounced,
202 consequently, there is no significant core complex exhumation. By 15 Myr, the
203 widespread distribution of shallow dipping normal faults across the entire crust does
204 not develop, unlike in EXP-1, such fault plane rotation is very limited. The Moho
205 variation remains subdued throughout the entire model domain and the strain
206 localization mechanism may be characterized by wide rift type, in the sense defined
207 by Buck (1991) and shown in numerical experiments of Brune et al., (2017).

208 On the other hand, with an increased extension velocity ($V_{ext} = 4$ cm/yr) in
209 EXP-3, strain localization, ductile flow, and the associated exhumation of
210 metamorphic cores and dome-like structures are accelerated (Figure 4b). For instance,

211 by 5 Myr there is up to ~ 20 km lower crustal exhumation between closely spaced
212 faults associated with shallow dip angles near the surface. By 10 Myr, the lower crust
213 reaches the surface at the left limb of the symmetrically arranged detachment faults.
214 Results show similarities with that of EXP-1, for example, oppositely dipping
215 detachment systems warping around domal cores, however, the entire evolution
216 develops much more rapidly. Note that the crustal thickness varies significantly
217 across the model domain, for instance, it is undulated and thinned around the margins,
218 nevertheless, the crustal thickness is almost constant beneath bivergent detachments
219 where the upper crustal thinning is more amplified and the crustal flow process
220 controls isostatic compensation.

221 In Figure 4c we show the evolution of EXP-4 in which the strength of the
222 upper crust is reduced by amplifying the frictional plastic strain softening. The
223 motivation for such parameter change comes from previous studies where Huisman
224 and Beaumont (2002) suggest that extensional tectonics may be symmetric or
225 asymmetric depending on the implementation of this variable. By 6 Myr, instead of
226 conjugate shear zone development, strain localizes along a specific shear zone, such
227 as the one on the right side of the model where asymmetry prevails in earlier stages of
228 the extension (Huisman and Beaumont, 2002). After 15 Myr, the unroofing of the
229 metamorphic dome reaches ~5 km depth below the surface as the deformation pattern
230 becomes distinctly asymmetric by the development of a detachment zone across the
231 brittle crust on the domed limb. This is similar to the simple shear extension model of
232 Wernicke (1985), but a major detachment in our model soles in the lower crust rather
233 than cutting through the lithosphere. Depending on the investigated width of the
234 model domain, such extension type may also be symmetrical in terms of detachment
235 fault development (Grasemann et al., 2012). Namely, another low-angle high strain

236 shear zone develops (not shown in this frame), dipping in the opposite direction to the
237 main shear zone, but it is in the distal end of the frame, 300 km further away from it.
238 Although footwall rotation and the differential uplift of the lower crust are well
239 pronounced in this experiment, we note that the results of EXP-4 do not account for
240 the observed tectonics of the central Menderes region. For example, EXP-4 does not
241 predict <100 km distance between Alaşehir/Gediz and Büyük Menderes detachment
242 faults, symmetrical exhumation of metamorphic cores, and the flat Moho between
243 these faults, inferred from seismological studies (e.g., Zhu et al., 2006; Fichtner et al.,
244 2013; Karabulut et al., 2013).

245 **4. Discussion**

246 The results of the reference numerical experiment (EXP-1), where lower
247 crustal flow is associated with footwall exhumation of “twin-domes” and rotation of
248 steep normal faults in the upper crust into two major shallow-dipping high strain
249 zones, comprise many of the first-order features that are invoked to explain the
250 tectonic evolution of the central Menderes metamorphic core complex in western
251 Anatolia. Figure 5a illustrates the spatial and structural agreement between the
252 predicted bivergent tectonics in the form of an observed present-day axisymmetric
253 array of low-angle shear zones projected across an N-S cross section of the region
254 (see Fig 1a X-X’ for the location of the cross section). Further, the results satisfy the
255 approximate distance between the Gediz (Alaşehir) (north) and Büyük Menderes
256 (south) detachment faults and associated flanking and exhumation of “twin-domes
257 shaped” footwall metamorphic rocks (Rey et al., 2011; Whitney et al., 2015).
258 Moreover, the simulated geometry approximates the syncline/downward arc beneath
259 Küçük Menderes graben in the center, with both detachments lying on the margin of
260 this syncline. As the model predicts, there is no known detachment fault associated

261 with the formation of Küçük Menderes (axial) graben where high-angle normal faults
262 control its evolution since the Middle Miocene (Emre and Sözbilir, 2007; Rojay et al.,
263 2005; Seyitoğlu and Işık, 2009; Bozkurt et al., 2008), similar to the formation of a
264 localized and narrow rift in the distributed extensional domain (Brun and
265 Choukroune, 1983).

266 Our model findings show that high-angle normal faults (50°-55°) have rotated
267 progressively ~40° to shallower dips about a horizontal axis accommodated by the
268 crustal flow. This is consistent with several geological interpretations in western
269 Anatolia. Namely, by interpreting the thermochronology data, cooling ages, and
270 reconstruction of Eocene (flat) foliation planes to present day tilted structures,
271 Gessner et al. (2001) suggest that the dip angle of both Gediz (Alaşehir) and Büyük
272 Menderes detachment faults were initially 40°-60° during the earlier stages of post-
273 Alpine extension. The higher dip angle origin of both Gediz (Alaşehir) and Büyük
274 Menderes low-angle detachment faults has also been suggested through current (non-
275 horizontal/tilted) dip angles of the bedding planes of syn-tectonic sedimentary strata,
276 dipping towards the fault plane (Bozkurt, 2000; Sözbilir, 2001; Seyitoğlu et al 2002;
277 Sümer et al., 2000; Çiftçi and Bozkurt, 2010; Türesin et al., 2021). According to fault
278 plane restoration estimates, based on vertical distributed shear (Westaway and
279 Kusznir (1993)) that develops contemporaneously with crustal extension and
280 sedimentary deposition, the initial dip angle of the Büyük Menderes detachment
281 ranges from 44° to 54° (Bozkurt, 2000), and an original dip of 56°-58° was estimated
282 for the Gediz/Alaşehir detachment (Cohen et al., 1995). We note that during the
283 model evolution a younger higher-angle normal fault forms on the hanging-wall of
284 the low-angle detachment akin to rider blocks (Reston and Ranero, 2011; Choi and
285 Buck, 2012). This new steeply dipping splay fault merges with the major detachment

286 along the brittle-ductile transition while its dip angle reduces through time. In EXP-1
287 such a fault system starts to develop 12 Myr after model initiation, (e.g., comparable
288 to 3-4 Ma before present in central Menderes geological evolution). The timing is in
289 accord with the onset of higher-angle normal faults and the deposition of Late
290 Miocene-Pliocene sediments proximal to the margin of the Gediz and Büyük
291 Menderes grabens (Sarica, 2000; Bozkurt and Sözbilir, 2004; Kent et al., 2016).

292 Short wavelength (≤ 150 km) variations of the crustal structures across the
293 central Menderes Massif region are shown in Figure 5b based on a regional high-
294 resolution seismic tomography model (Fichtner et al., 2013). Notably, slow seismic
295 velocities ($V_s < 3.4$ km/s, < 20 km depths, light blue region) in the upper part of the
296 crust are observed in the center, beneath the Küçük Menderes graben to which lower
297 crustal exhumation and detachment faulting have not been ascribed. However, on
298 both margins of the Küçük Menderes graben, there are higher seismic velocities (3.4
299 $\leq V_s \leq 3.8$ km/s black and yellow regions) at shallower depths associated with the
300 uprising of the lower crust (Fichtner et al., 2013; Çubuk-Sabuncu et al., 2017). This is
301 consistent with findings of the EXP-1, where a twin-domes feature develops by
302 crustal flow (Fig. 5a).

303 In Figure 5a, we show the predicted Moho depth variation and it is sub-
304 horizontal beneath the central Menderes Massif region where the Moho depth ranges
305 from 25 to 28 km. Results of EXP-1 are mainly consistent with seismologically
306 derived Moho variations for this part of western Anatolia's extended terrane (Zhu et
307 al., 2006; Karabulut et al., 2013; Fichtner et al., 2013). It is worth noting that Moho
308 beneath western Anatolia shows undulated pattern along the N-S transect, however, it
309 is locally flat underneath the Menderes Massif. (Karabulut et al., 2013). Again, the
310 flat Moho is controlled by the ductile flow of the mid-lower crust to isostatically

311 compensate for the differential thinning of the upper crust and variations in crustal
312 thickness, and this process has been suggested to account for the evolution of
313 cordilleran core complexes in the western US and the Aegean region (Klemperer et al.,
314 1986; Gans, 1987; Block and Royden, 1990; McKenzie et al., 2000; Tirel et al.,
315 2004).

316 In Figure 5c, we reconcile the exhumation history of the central Menderes
317 Massif derived from low temperature thermochronological constraints against the
318 predictions of EXP-1. For EXP-1, the exhumation rates are calculated (for every 1
319 Myr) through the trajectory of the lower crust at minimum depths with respect to the
320 zero elevation (see yellow dots shown in the figure inset). These points on both domes
321 correspond to the exhumed crust beneath the two detachment faults and follow
322 approximately similar patterns and magnitudes since the beginning of the model (with
323 uncertainties of ± 0.2 km/My). Namely, there is an increase in the exhumation rate
324 between 15- 10 Ma, from 1 km/My to ~ 1.7 km/My and then it starts to decrease to
325 ~ 0.6 km/My by 5 Ma. The change after 5-0 is relatively minor and it is > 1.0 km/My.
326 Two-stage evolution predicted by the EXP-1 is in accord with the findings of Wölfler
327 et al. (2017) for the exhumation of the footwall rocks of the Büyük Menderes
328 detachment. According to the authors, the exhumation rate is ~ 0.9 km/My during
329 middle Miocene and it decreases to ~ 0.43 km/My during the Miocene to Pliocene.
330 For the footwall rocks of the Gediz detachment, Buscher et al. (2013) estimates that
331 the rate of exhumation is 0.6-2 km/My and such variation is in the range of our model
332 calculations.

333 We note that our models do not account for all geological processes involved
334 in the late Cenozoic evolution of western Anatolia, such as surface erosion, partial

335 melting of the lower crust, and plate rotation. For instance, based on
336 thermochronological data and available erosion rates, Buscher et al. (2013) suggest
337 that surface erosion also controls the exhumation and the landscape evolution of the
338 Bozdağ block, an exhumed range displaced by the Gediz detachment fault. Recent
339 cosmogenic nuclides study by Heineke et al. (2019a) suggests that the erosion plays
340 relatively minor role for rock exhumation along Gediz and Büyük Menderes (~10%
341 for the Gediz), however, it is more effective along both sides of the Küçük Menderes
342 graben (~50% rock exhumation). In our models, the flow of the lower crust, hence,
343 the double dome formation (footwall exhumation) is mainly controlled by isostasy
344 rather than lower crustal buoyancy. Rey et al. (2011) presents numerical experiments
345 where partially molten lower crust becomes buoyant and double dome formation
346 occurs with a small magnitude of extensional strain rate. Buoyancy driven dome
347 formation may apply some of the cordilleran type metamorphic core complexes in
348 North America where regional extension is decoupled from lower crustal flow under
349 pure shear extension (Levy et al., 2023; Zuza and Cao, 2022). Although it may exert
350 control to some degree, the purely buoyancy driven crustal upwelling model does not
351 apply to the Aegean-west Anatolia, because the lithospheric extension in the region
352 has been active since ~25 Ma (Seyitoğlu et al 1996; Bozkurt and Sözbilir, 2004;
353 Çemen et al., 2006; Gessner et al., 2013; Roche et al., 2018; Heineke et al 2019a,b).
354 In brief, the isostatic footwall uplift by stretching is the primary mechanism driving
355 twin dome formation in the area as predicted by our experiments in this work.
356 Further, van Hinsbergen et al. (2010a) provides paleomagnetic evidence for a vertical
357 axis rotation of ~25°-30° in the central Menderes region with respect to the northern
358 and southern part of the Menderes Massif to account for crustal exhumation and
359 detachment faulting since ~16 Ma. This would certainly be the focus of future 3-D

360 modeling studies. Overall, the results of our reference experiment (EXP-1) are
361 consistent with the present-day flat Moho inferred from seismological studies as well
362 as with the twin-dome type exhumed massifs along bivergent detachment faults as
363 documented by geological studies.

364 The exhumation of metamorphic core complexes and associated low-angle
365 normal faults are common features of large-magnitude extensional provinces across
366 Cordilleran and Mediterranean regions that develop in the terminal phase or in the
367 aftermath of orogenesis. The results of this work in which progressive rotation of the
368 high-angle normal faults to low-angle orientations as well as the exhumation of
369 symmetrical (twin) domes are accommodated by the distributed flow of the lower
370 crust may explain how post-orogenic lithospheric extension operates around the
371 globe.

372 **References**

- 373 Aktuğ, B., Nocquet, J., Cingöz, A., Parsons, B., Erkan, Y., England, P., Lenk, O.,
374 Gürdal, M., Kilicoglu, A., Akdeniz, H., et al., 2009. Deformation of western
375 Turkey from a combination of permanent and campaign GPS data: Limits to
376 block-like behavior. *Journal of Geophysical Research: Solid Earth* 114.
- 377 Aldanmaz, E., Pearce, J.A., Thirlwall, M., Mitchell, J., 2000. Petrogenetic evolution
378 of late Cenozoic, post-collision volcanism in western Anatolia, Turkey. *Journal of*
379 *volcanology and geothermal research* 102, 67–95.
- 380 Bangerth, W., Dannberg, J., Gassmoeller, R., Heister, T., 2020. Aspect v2. 2.0.
381 Zenodo.
- 382 Block, L., Royden, L.H., 1990. Core complex geometries and regional scale flow in
383 the lower crust. *Tectonics* 9, 557–567.
- 384 Bozkurt, E., 2000. Timing of extension on the Büyük Menderes graben, western
385 Turkey, and its tectonic implications. *Geological Society, London, Special*
386 *Publications* 173, 385–403.
- 387 Bozkurt, E., 2001. Late alpine evolution of the central Menderes massif, western
388 Turkey. *International Journal of Earth Sciences* 89, 728–744.
- 389 Bozkurt, E., Sözbilir, H., 2004. Tectonic evolution of the Gediz graben: field evidence
390 for an episodic, two-stage extension in western Turkey. *Geological Magazine* 141,
391 63–79.
- 392 Bozkurt, E., Winchester, J.A., Ruffet, G., Rojay, B., 2008. Age and chemistry of
393 miocene volcanic rocks from the Kiraz Basin of the Küçük Menderes graben: Its
394 significance for the extensional tectonics of southwestern Anatolia, Turkey.
395 *Geodinamica Acta* 21, 239–257.
- 396 Brun, J.P., Choukroune, P., 1983. Normal faulting, block tilting, and decollement in a
397 stretched crust. *Tectonics* 2, 345–356.
- 398 Brune, S., Heine, C., Clift, P.D., Pérez-Gussinyé, M., 2017. Rifted margin
399 architecture and crustal rheology: reviewing Iberia-newfoundland, central south
400 Atlantic, and south China sea. *Marine and Petroleum Geology* 79, 257–281.
- 401 Buck, W.R., 1988. Flexural rotation of normal faults. *Tectonics* 7, 959–973.
- 402 Buck, W.R., 1991. Modes of continental lithospheric extension. *Journal of*
403 *Geophysical Research: Solid Earth* 96, 20161–20178.

404 Buscher, J., Hampel, A., Hetzel, R., Dunkl, I., Glotzbach, C., Struffert, A., Akal, C.,
405 Ratz, M., 2013. Quantifying rates of detachment faulting and erosion in the
406 central Menderes massif (western Turkey) by thermochronology and cosmogenic
407 ¹⁰be. *Journal of the Geological Society* 170, 669–683.

408 Catlos, E., Çemen, I., 2005. Monazite ages and the evolution of the Menderes massif,
409 western Turkey. *International Journal of Earth Sciences* 94, 204–217.

410 Çemen, I., Catlos, E.J., Göğüş, O., Özerdem, C., 2006. Postcollisional extensional
411 tectonics and exhumation of the Menderes massif in the western Anatolia
412 extended terrane, Turkey.

413 Choi, E., Buck, W.R., 2012. Constraints on the strength of faults from the geometry
414 of rider blocks in continental and oceanic core complexes. *Journal of Geophysical
415 Research: Solid Earth* 117.

416 Çiftçi, N., Bozkurt, E., 2010. Structural evolution of the Gediz graben, SW Turkey:
417 temporal and spatial variation of the graben basin. *Basin research* 22, 846–873.

418 Cohen, H., Dart, C., Akyüz, H., Barka, A., 1995. Syn-rift sedimentation and structural
419 development of the Gediz and Büyük Menderes graben, western turkey. *Journal of
420 the Geological Society* 152, 629–638.

421 Çubuk-Sabuncu, Y., Taymaz, T., Fichtner, A., 2017. 3-d crustal velocity structure of
422 western Turkey: Constraints from full-waveform tomography. *Physics of the
423 Earth and Planetary Interiors* 270, 90–112.

424 Demircioğlu, D., Ecevitoglu, B., Seyitoğlu, G., 2010. Evidence of a rolling hinge
425 mechanism in the seismic records of the hydrocarbon-bearing Alaşehir graben,
426 western Turkey.

427 Dewey, J.F., 1988. Extensional collapse of orogens. *Tectonics* 7, 1123–1139.

428 Dinç Göğüş, Ö., Avşar, E., Develi, K., Çalık, A., 2023. Quantifying the rock damage
429 intensity controlled by mineral compositions: insights from fractal analyses.
430 *Fractal Fract.* 7 (5), 383.

431 Emre, T., Sözbilir, H., 2007. Tectonic evolution of the Kiraz Basin, Küçük Menderes
432 graben: evidence for compression/uplift-related basin formation overprinted by
433 extensional tectonics in west Anatolia. *Turkish Journal of Earth Sciences* 16, 441–
434 470.

435 Emre, T., Sözbilir, H., 1997. Field evidence for metamorphic core complex,
436 detachment faulting and accommodation faults in the Gediz and Büyük Menderes
437 grabens, western Anatolia. *Iesca Proceedings* 1, 73–93.

438 Ersoy, E.Y., Helvacı, C., Palmer, M.R., 2010. Mantle source characteristics and
439 melting models for the early-middle Miocene mafic volcanism in western
440 Anatolia: implications for enrichment processes of mantle lithosphere and origin
441 of k-rich volcanism in post-collisional settings. *Journal of Volcanology and*
442 *Geothermal Research* 198, 112–128.

443 Fichtner, A., Trampert, J., Cupillard, P., Saygin, E., Taymaz, T., Capdeville, Y.,
444 Villasenor, A., 2013. Multiscale full waveform inversion. *Geophysical Journal*
445 *International* 194, 534–556.

446 Gans, P.B., 1987. An open-system, two-layer crustal stretching model for the eastern
447 great basin. *Tectonics* 6, 1–12.

448 Gessner, K., Gallardo, L.A., Markwitz, V., Ring, U., Thomson, S.N., 2013. What
449 caused the denudation of the Menderes Massif: Review of crustal evolution,
450 lithosphere structure, and dynamic topography in southwest turkey. *Gondwana*
451 *research* 24, 243–274.

452 Gessner, K., Ring, U., Johnson, C., Hetzel, R., Passchier, C.W., Güngör, T., 2001. An
453 active bivergent rolling-hinge detachment system: Central menderes metamorphic
454 core complex in western Turkey. *Geology* 29, 611– 614.

455 Gleason, G.C., Tullis, J., 1995. A flow law for dislocation creep of quartz aggregates
456 determined with the molten salt cell. *Tectonophysics* 247, 1–23.

457 Glerum, A., Thieulot, C., Fraters, M., Blom, C., Spakman, W., 2018. Non- linear
458 viscoplasticity in aspect: benchmarking and applications to subduction. *Solid*
459 *Earth* 9, 267–294.

460 Glodny, J., Hetzel, R., 2007. Precise u–pb ages of syn-extensional Miocene intrusions
461 in the central menderes massif, western turkey. *Geological Mag-*
462 *azine* 144, 235–
246.

463 Grasemann, B., Schneider, D.A., Stöckli, D.F., Iglseider, C., 2012. Miocene bivergent
464 crustal extension in the Aegean: Evidence from the western Cyclades (Greece).
465 *Lithosphere* 4, 23–39.

466 Göğüş, O. H., 2015. Rifting and subsidence following lithospheric removal in
467 continental back arcs. *Geology*, 43(1), 3-6.

468 Göğüş, O.H., 2004. Geometry and Tectonic Significance of Büyük Menderes
469 Detachment, in the Bascayir Area, Büyük Menderes Graben, Western Turkey.
470 Ph.D. thesis. Oklahoma State University.

471 Heineke, C., Hetzel, R., Nilius, N.P., Glotzbach, C., Akal, C., Christl, M., Hampel,
472 A., 2019a. Spatial patterns of erosion and landscape evolution in a bivergent
473 metamorphic core complex revealed by cosmogenic ¹⁰be: The central Menderes
474 Massif (western Turkey). *Geosphere* 15, 1846–1868.

475 Heineke, C., Hetzel, R., Nilius, N.P., Zwingmann, H., Todd, A., Mulch, A., Wölfler,
476 A., Glotzbach, C., Akal, C., Dunkl, I., et al., 2019b. Detachment faulting in a
477 bivergent core complex constrained by fault gouge dating and low-temperature
478 thermochronology. *Journal of Structural Geology* 127, 103865.

479 Heister, T., Dannberg, J., Gassmüller, R., Bangerth, W., 2017. High accuracy mantle
480 convection simulation through modern numerical methods–ii: realistic models and
481 problems. *Geophysical Journal International* 210, 833–851.

482 Hetzel, R., Passchier, C.W., Ring, U., Dora, O., 1995. Bivergent extension in
483 orogenic belts: the Menderes Massif (southwestern Turkey). *Geology* 23, 455–
484 458.

485 Hetzel, R., Zwingmann, H., Mulch, A., Gessner, K., Akal, C., Hampel, A., Güngör,
486 T., Petschick, R., Mikes, T., Wedin, F., 2013. Spatiotemporal evolution of brittle
487 normal faulting and fluid infiltration in detachment fault systems: A case study
488 from the Menderes Massif, western Turkey. *Tectonics* 32, 364–376.

489 Hirth, G., Kohlstedt, D., 2003. Rheology of the upper mantle and the mantle wedge:
490 A view from the experimentalists. *Geophysical monograph- American*
491 *geophysical union* 138, 83–106.

492 Huismans, R.S., Beaumont, C., 2002. Asymmetric lithospheric extension: The role of
493 frictional plastic strain softening inferred from numerical experiments. *Geology*
494 30, 211–214.

495 Huismans, R.S., Beaumont, C., 2003. Symmetric and asymmetric lithospheric
496 extension: Relative effects of frictional-plastic and viscous strain softening.
497 *Journal of Geophysical Research: Solid Earth* 108.

498 Işık, V., Seyitoğlu, G., Çemen, I., 2003. Ductile–brittle transition along the Alaşehir
499 detachment fault and its structural relationship with the Simav detachment fault,
500 Menderes Massif, western Turkey. *Tectonophysics* 374, 1–18.

501 Jolivet, L., 2001. A comparison of geodetic and finite strain pattern in the Aegean,
502 geodynamic implications. *Earth and Planetary science letters* 187, 95–104.

503 Jolivet, L., Brun, J.P., 2010. Cenozoic geodynamic evolution of the Aegean.
504 *International Journal of Earth Sciences* 99, 109–138.

505 Karabulut, H., Paul, A., Afacan Ergün, T., Hatzfeld, D., Childs, D.M., Aktar, M.,
506 2013. Long-wavelength undulations of the seismic moho beneath the strongly
507 stretched western anatolia. *Geophysical Journal International* 194, 450–464.

508 Kent, E., Boulton, S., Stewart, I., Whittaker, A., Alçiçek, M.C., 2016. Geomorphic
509 and geological constraints on the active normal faulting of the Gediz (Alaşehir)
510 graben, western turkey. *Journal of the Geological Society* 173, 666–678.

511 Klemperer, S.L., Hauge, T., Hauser, E., Oliver, J., Potter, C., 1986. The moho in the
512 northern basin and range province, Nevada, along the cocorp 40 n seismic-
513 reflection transect. *Geological Society of America Bulletin* 97, 603–618.

514 Kronbichler, M., Heister, T., Bangerth, W., 2012. High accuracy mantle convection
515 simulation through modern numerical methods. *Geophysical Journal International*
516 191, 12–29.

517 Le Pourhiet, L., May, D.A., Huille, L., Watremez, L., Leroy, S., 2017. A genetic link
518 between transform and hyper-extended margins. *Earth and Planetary Science*
519 *Letters* 465, 184–192.

520 Levy, D.A., Zuza, A.V., Michels, Z.D., DesOrmeau, J.W., 2023. Buoyant doming
521 generates metamorphic core complexes in the north American cordillera. *Geology*
522 51, 290–294.

523 Lips, A.L., Cassard, D., Sözbilir, H., Yilmaz, H., Wijbrans, J., 2001. Multi- stage
524 exhumation of the Menderes massif, western Anatolia (Turkey). *International*
525 *Journal of Earth Sciences* 89, 781–792.

526 Lister, G.S., Banga, G., Feenstra, A., 1984. Metamorphic core complexes of
527 Cordilleran type in the Cyclades, Aegean Sea, Greece. *Geology* 12 (4), 221–225.

528 Malavieille, J., 1993. Late orogenic extension in mountain belts: insights from the
529 basin and range and the late paleozoic variscan belt. *Tectonics* 12, 1115–1130.

530 McKenzie, D., Nimmo, F., Jackson, J.A., Gans, P., Miller, E., 2000. Characteristics
531 and consequences of flow in the lower crust. *Journal of Geophysical Research:*
532 *Solid Earth* 105, 11029–11046.

533 Nilius, N.P., Glotzbach, C., Wölfler, A., Hampel, A., Dunkl, I., Akal, C., Heineke, C.,
534 Hetzel, R., 2019. Exhumation history of the Aydın range and the role of the
535 Büyük Menderes detachment system during bivergent extension of the central
536 Menderes massif, western turkey. *Journal of the Geological Society* 176, 704–
537 726.

538 Okay, A.I., 2001. Stratigraphic and metamorphic inversions in the central Menderes
539 massif: a new structural model. *International Journal of Earth Sciences* 89, 709–
540 727.

541 Öner, Z., Dilek, Y., 2011. Supradetachment basin evolution during continental
542 extension: The Aegean province of western Anatolia, Turkey. *Bulletin* 123, 2115–
543 2141.

544 Reston, T., Ranero, C.R., 2011. The 3-d geometry of detachment faulting at mid-
545 ocean ridges. *Geochemistry, Geophysics, Geosystems* 12.

546 Rey, P., Vanderhaeghe, O., Teyssier, C., 2001. Gravitational collapse of the
547 continental crust: definition, regimes and modes. *Tectonophysics* 342, 435–449.

548 Rey, P.F., Teyssier, C., Kruckenberg, S.C., Whitney, D.L., 2011. Viscous collision in
549 channel explains double domes in metamorphic core complexes. *Geology* 39,
550 387–390.

551 Ring, U., Johnson, C., Hetzel, R., Gessner, K., 2003. Tectonic denudation of a late
552 cretaceous–tertiary collisional belt: regionally symmetric cooling patterns and
553 their relation to extensional faults in the Anatolide belt of western Turkey.
554 *Geological Magazine* 140, 421–441.

555 Roche, V., Conand, C., Jolivet, L., Augier, R., 2018. Tectonic evolution of Leros
556 (Dodecanese, Greece) and correlations between the Aegean domain and the
557 Menderes massif. *Journal of the Geological Society* 175, 836–849.

558 Rojay, B., Toprak, V., Demirci, C., Süzen, L., 2005. Plio-quadernary evolution of the
559 Küçük Menderes graben southwestern Anatolia, turkey. *Geodinamica Acta* 18,
560 317–331.

561 Rose, I., Buffett, B., Heister, T., 2017. Stability and accuracy of free surface time
562 integration in viscous flows. *Physics of the Earth and Planetary Interiors* 262, 90–
563 100.

564 Rossetti, F., Asti, R., Faccenna, C., Gerdes, A., Lucci, F., Theye, T., 2017.
565 Magmatism and crustal extension: Constraining activation of the ductile shearing
566 along the Gediz detachment, Menderes massif (western Turkey). *Lithos* 282, 145–
567 162.

568 Rybacki, E., Dresen, G., 2000. Dislocation and diffusion creep of synthetic anorthite
569 aggregates. *Journal of Geophysical Research: Solid Earth* 105, 26017–26036.

570 Sarica, N., 2000. The plio-pleistocene age of Büyük Menderes and Gediz grabens and
571 their tectonic significance on n-s extensional tectonics in west Anatolia:
572 mammalian evidence from the continental deposits. *Geological journal* 35, 1–24.

573 Şen, S., Seyitoğlu, G., 2009. Magnetostratigraphy of early–middle Miocene deposits
574 from east–west trending Alaşehir and Büyük Menderes grabens in western
575 Turkey, and its tectonic implications. *Geological Society, London, Special
576 Publications* 311, 321–342.

577 Şengör, A., Görür, N., Şarağlı, F., 1985. Strike-slip faulting and related basin
578 formation in zones of tectonic escape: Turkey as a case study.

579 Seyitoğlu, G., Tekeli, O., Çemen, I., Şen, Ş., & Işık, V. 2002. The role of the flexural
580 rotation/rolling hinge model in the tectonic evolution of the Alaşehir graben,
581 western t,Turkey. *Geological Magazine* 139, 15–26.

582 Seyitoglu, V.G., Işık, V., 2009. Meaning of the Küçük Menderes graben in the
583 tectonic framework of the central Menderes metamorphic core complex (western
584 Turkey). *Geologica Acta* 7, 323–332.

585 Seyitoğlu, G., Işık, V., Çemen, I., 2004. Complete tertiary exhumation his- tory of the
586 Menderes massif, western turkey: an alternative working hypothesis. *Terra Nova*
587 16, 358–364.

588 Seyitoğlu, G., Scott, B.C., 1996. The cause of ns extensional tectonics in western
589 turkey: tectonic escape vs back-arc spreading vs orogenic collapse. *Journal of
590 Geodynamics* 22, 145–153.

591 Sözbilir, H., 2001. Extensional tectonics and the geometry of related macroscopic
592 structures: field evidence from the Gediz detachment, western turkey. *Turkish
593 Journal of Earth Sciences* 10, 51–67.

594 Sümer, Ö., Sözbilir, H., Bora, U., 2020. Büyük Menderes grabeni'nin rolling hinge
595 (yuvarlanan reze) modelinde supra-detachment (sıyrılma üstü) havzadan rift
596 havzasına evrimi. *Türkiye Jeoloji Bu 'lteni* 63, 241– 276.

597 Tirel, C., Gueydan, F., Tiberi, C., Brun, J.P., 2004. Aegean crustal thick- ness inferred
598 from gravity inversion. geodynamical implications. *Earth and Planetary Science
599 Letters* 228, 267–280.

600 Türesin, F.M., Seyitoğlu, G., 2021. Alaşehir type-rolling hinge mechanism in the
601 northern margin of Büyük Menderes graben: Evidence from seismic reflection
602 and recent thermochronological data. *Turkish Journal of Earth Sciences* 30, 322–
603 340.

604 van Hinsbergen, D.J., Dekkers, M.J., Bozkurt, E., Koopman, M., 2010a. Exhumation
605 with a twist: Paleomagnetic constraints on the evolution of the Menderes
606 metamorphic core complex, western Turkey. *Tectonics* 29.

607 van Hinsbergen, D.J., Kaymakci, N., Spakman, W., Torsvik, T.H., 2010b.
608 Reconciling the geological history of western Turkey with plate circuits and
609 mantle tomography. *Earth and Planetary Science Letters* 297, 674–686.

610 Wernicke, B., 1985. Uniform-sense normal simple shear of the continental
611 lithosphere. *Canadian Journal of Earth Sciences* 22, 108–125.

612 Wernicke, B., Axen, G.J., 1988. On the role of isostasy in the evolution of normal
613 fault systems. *Geology* 16, 848–851.

614 Westaway, R., Kusznir, N., 1993. Fault and bed ‘rotation’ during continental
615 extension: block rotation or vertical shear? *Journal of Structural Geology* 15, 753–
616 770.

617 Whitney, D.L., Roger, F., Teyssier, C., Rey, P.F., Respaut, J.P., 2015. Syn-collapse
618 eclogite metamorphism and exhumation of deep crust in a migmatite dome: The
619 p–t record of the youngest variscan eclogite (Montagne Noire, Trench massif
620 central). *Earth and Planetary Science Letters* 430, 224–234.

621 Wölfler, A., Glotzbach, C., Heineke, C., Nilius, N.P., Hetzel, R., Hampel, A., Akal,
622 C., Dunkl, I., Christl, M., 2017. Late Cenozoic cooling history of the central
623 Menderes massif: Timing of the Büyük Menderes detachment and the relative
624 contribution of normal faulting and erosion to rock exhumation. *Tectonophysics*
625 717, 585–598.

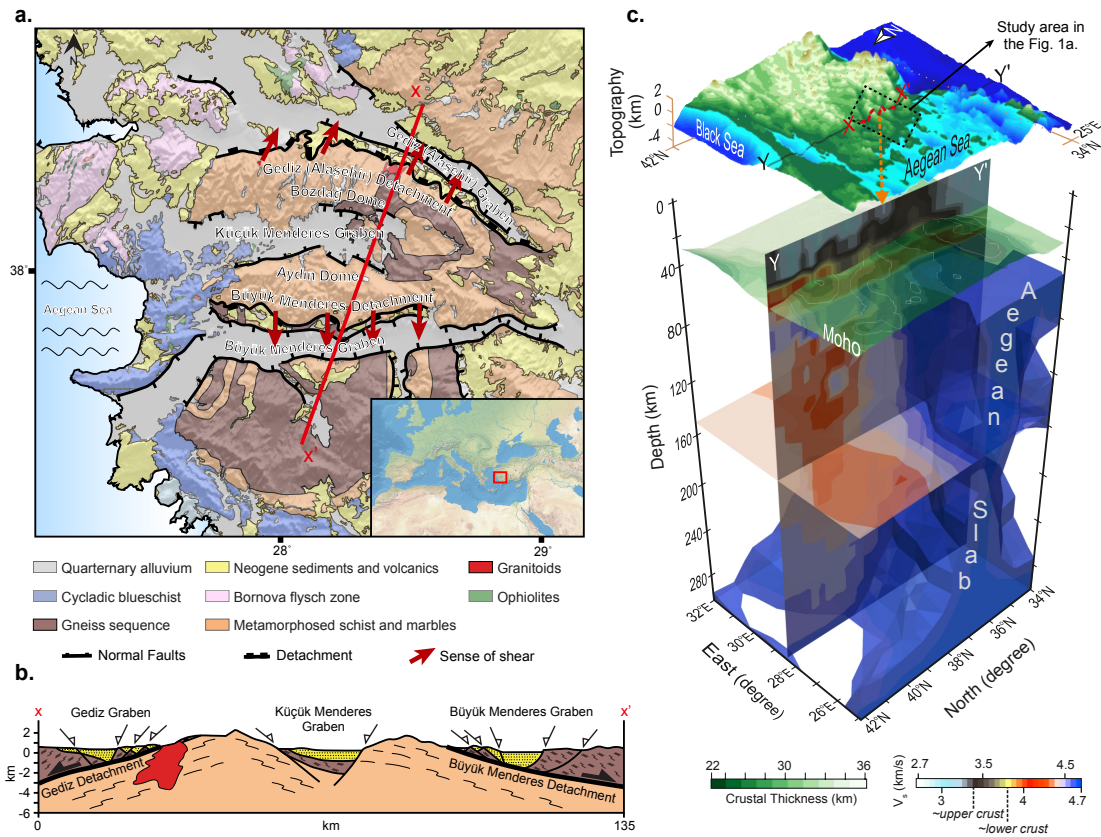
626 Zhu, L., Mitchell, B.J., Akyol, N., Cemen, I., Kekovali, K., 2006. Crustal thickness
627 variations in the Aegean region and implications for the extension of continental
628 crust. *Journal of Geophysical Research: Solid Earth* 111.

629 Zuza, A., Cao, W., 2022. Metamorphic core complex dichotomy in the north
630 american cordillera explained by buoyant upwelling in variably thick crust. *GSA*
631 *Today*.

632

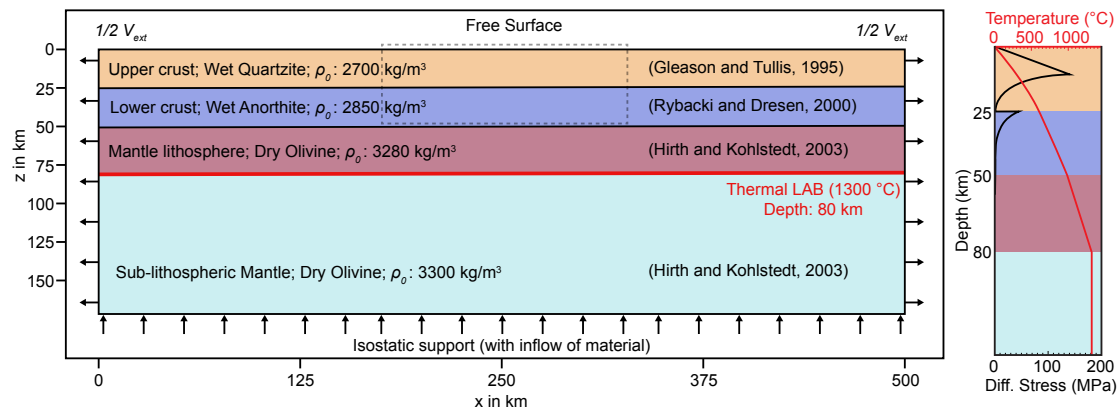
633 **Acknowledgements**

634 We thank the Computational Infrastructure for Geodynamics (geodynamics.org)
635 which is funded by the National Science Foundation under award EAR-0949446 and
636 EAR-1550901 for supporting the development of ASPECT. The numerical
637 experiments presented here are available through contacting the authors. Meanwhile,
638 documentation and the details for the numerical code can be found online (at
639 <https://aspect.geodynamics.org>). OHG, AF and EŞU acknowledge Anatolian
640 Tectonics Project-ANATEC (funded by Inter- national Lithosphere Program). The
641 authors gratefully acknowledge the computing time granted by the Resource
642 Allocation Board and provided on the supercomputer Lise at NHR@ZIB as part of
643 the NHR infrastructure. The calculations for this research were con- ducted with
644 computing resources under the project bbp00039. We are grateful to Paul Kapp and
645 an anonymous reviewer for their constructive comments on the manuscript. OHG
646 acknowledges Turkish Academy of Sciences (TUBA) for GEBIP support and
647 TUBITAK for 2219 fellowship programme. ACG is funded by a Helmholtz
648 Recruitment Initiative.
649



650

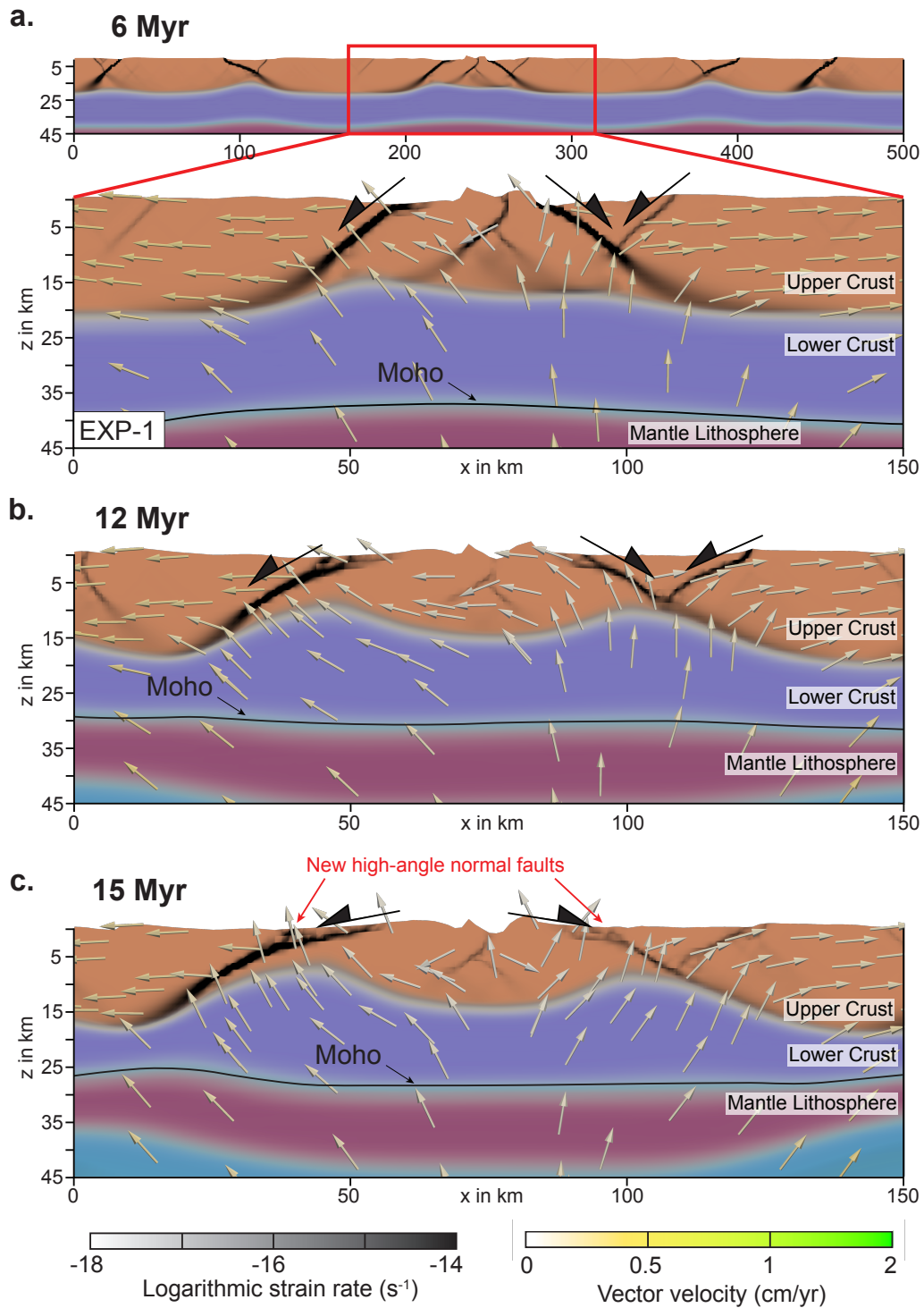
651 **Figure 1a.** Geological map of the central part of western Anatolia extensional region
 652 (Menderes Massif) that shows the main geological features discussed in this work.
 653 Metamorphosed schist and marble are footwall rocks and represented by greenschist
 654 to amphibolite facies metamorphics and the hangingwall rocks are described by high-
 655 grade metamorphics (Gneissic core). The map is based on the geological map of
 656 Türkiye (MTA, 2002), including the differentiation of metamorphic units, according
 657 to Lips et al (2001) and Okay (2001) **b.** Simplified NNE-SSW cross section across the
 658 central Menderes Massif that shows bivergent detachment faults and symmetrically
 659 arranged exhumed massifs **c.** 3-D view of a seismic tomography model based on
 660 isotropic S velocities (V_s) along the across the crust as well as the upper mantle
 661 beneath western Anatolia (derived from Fichtner et al., 2013).



662

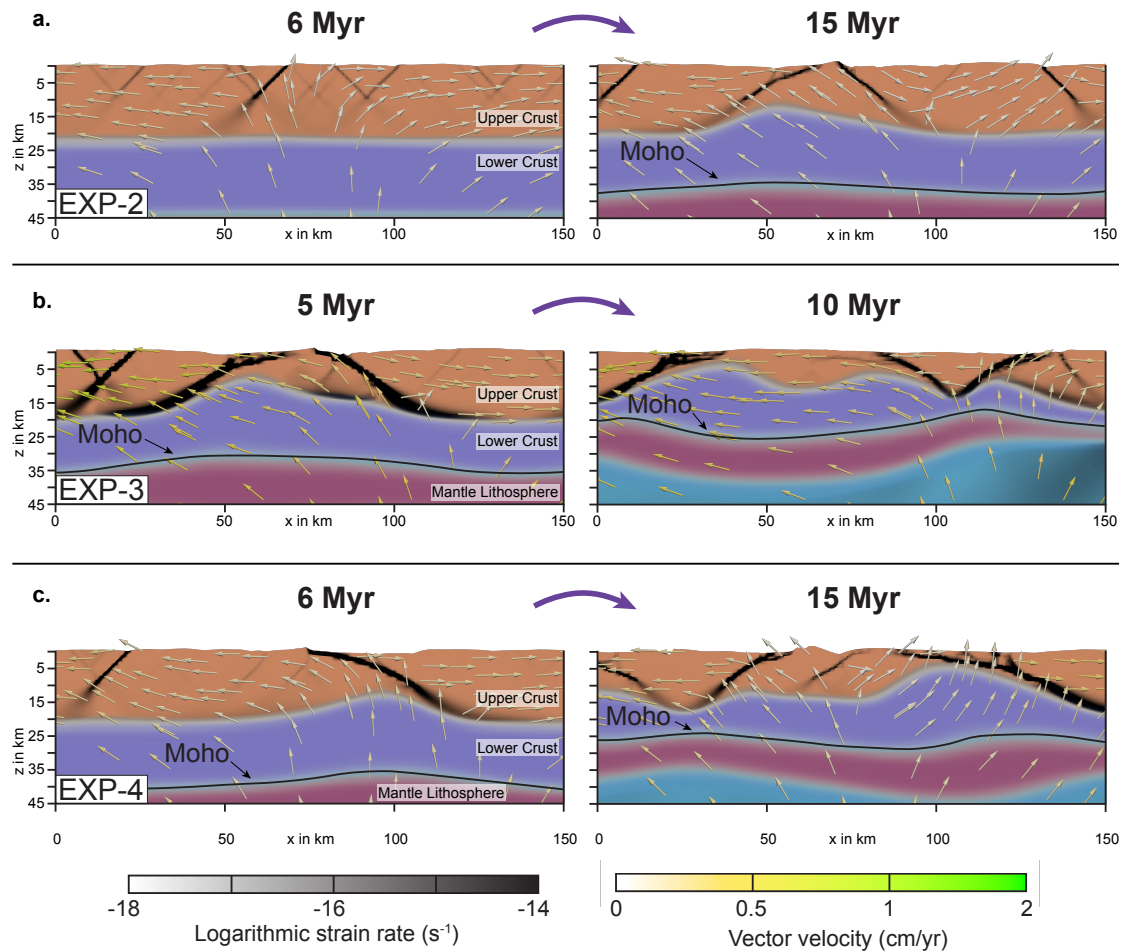
663 **Figure 2.** Illustration of the model geometry, set-up, material properties, and density
 664 fields for the experiments. The corresponding strength profile for the initial conditions
 665 and a strain rate of 1×10^{-15} is shown on the right. The dashed rectangle outlines the
 666 area shown in Figures 3 and 4. The density values given are the reference densities for
 667 each material.

668



669

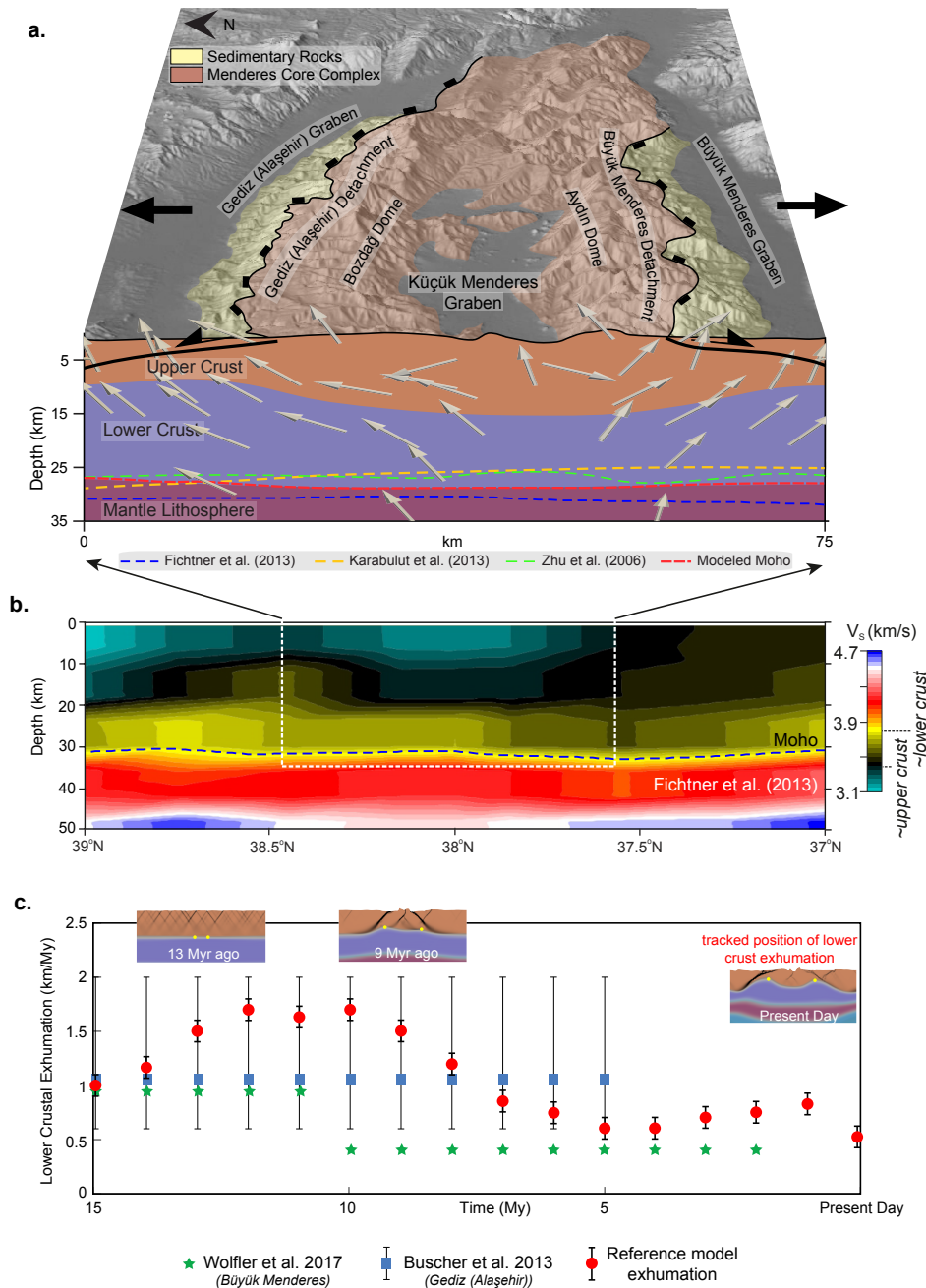
670 **Figure 3.** Geodynamic evolution of our reference experiment (EXP-1) that
 671 approximates the last 15 Myr geological evolution of the central Menderes Massif of
 672 western Anatolia. Note that central part of the model domain is shown (150 km wide).
 673 Strain localization is interpreted in accordance with shear zone development where
 674 footwall rotation is associated with detachment fault evolution. The vectors show
 675 flow field over the experiment.



676

677 **Figure 4.** Geodynamic evolution of EXP- 2, 3, and 4. All model parameters are kept
 678 constant with respect to the reference experiment (EXP-1) except, **a.** in EXP-2 the
 679 extension rate (1 cm/yr), **b.** in EXP-3 the extension rate (4 cm/yr), and **c.** in EXP-4 the
 680 upper crustal strength is reduced by decreasing the frictional weakening to 0.05.

681



682

683 **Figure 5.** Reconciling predictions of EXP-1 with geological, geophysical and
 684 thermochronological studies in the central Menderes massif of western Anatolia. **a.**
 685 NNE-SSW profile that shows the map projection of bivergent Gediz and Büyük
 686 detachment faults and their approximation to the model result. Note the agreement
 687 between modeled and observed Moho (see text for references). **b.** 2-D seismic (V_s)
 688 variations across the same profile of western Anatolia region to a depth of 50 km.
 689 Higher velocities in the shallow part of the crust (dark grey-black) are interpreted as
 690 the ascending of the normally associated lower crustal material. **c.** A diagram that
 691 shows the exhumation rate variation of the model and based on studies from low
 692 temperature thermochronology (Buscher et al., 2013 and Wölfler et al., 2017).

Parameter	Units	Upper Crust	Lower Crust	Lithospheric Mantle	Sub-Lithospheric Mantle
Reference Density	kgm^{-3}	2700	2850	3280	3300
Thermal expansivity	$10^{-5}K^{-1}$	2.7	2.7	3.0	3.0
Thermal diffusivity	$10^{-7}m^2s^{-1}$	7.7160	7.3099	8.3841	8.3333
Radiogenic heat production	μWm^3	1.5	0.2	-	-
Friction Weakening		0.1 and 0.05*	0.05	0.05	0.05
Cohesion strain weakening		0.05	0.05	0.05	0.05
<i>Rheology</i>		<i>Wet Quartzite</i>	<i>Wet Anorthite</i>	<i>Dry Olivine</i>	<i>Wet Olivine</i>
Pre-exponential constant for diffusion creep	$Pa^{-1}s^{-1}$	5.97×10^{-19}	2.99×10^{-25}	2.25×10^{-9}	2.25×10^{-9}
Grain size exponent		2.0	3.0	0	0
Activation energy for diffusion creep	$kJ mol^{-1}$	223	159	375	375
Activation volume for diffusion creep	$cm^3 mol^{-1}$	0	38.0	6.0	6.0
Pre-exponential constant for dislocation creep	$Pa^{-n}s^{-1}$	8.57×10^{-28}	7.13×10^{-18}	6.52×10^{-16}	6.52×10^{-16}
Power law exponent for dislocation creep		4.0	3.0	3.5	3.5
Activation energy for dislocation creep	$kJ mol^{-1}$	223	345	530	530
Activation volume for dislocation creep	$cm^3 mol^{-1}$	18.0	38.0	18.0	18.0

693

694 **Table 1:** Model parameters for reference experiment. *0.05 is used in experiment 4.

695 Initial parameters of temperature=293 K, adiabatic surface temperature=1557 K, heat

696 capacity=1200 Jkg⁻¹K⁻¹, internal friction angle=20°, cohesion=20 MPa, and grain

697 size=1 mm are defined in all layers.